Injection-limited and space charge-limited currents in organic semiconductor devices with nanopatterned metal electrodes

OPEN ACCESS
IOP Publishing
Nanotechnology

Nanotechnology **34** (2023) 035202 (9pp)
https://doi.org/10.1088/1361-6528/ac9686

Injection-limited and space charge-limited currents in organic semiconductor devices with nanopatterned metal electrodes

Janek Buhl[1,2], **Hannes Lüder**[1,2] and **Martina Gerken**[1,2,*]

[1] Chair for Integrated Systems and Photonics, Faculty of Engineering, Kiel University, Kaiserstraße 2, D-24143 Kiel, Germany
[2] Kiel Nano, Surface and Interface Science KiNSIS, Kiel University, Christian-Albrechts-Platz 4, D-24118 Kiel, Germany

E-mail: mge@tf.uni-kiel.de

Received 17 June 2022, revised 22 September 2022
Accepted for publication 30 September 2022
Published 4 November 2022

Abstract

Charge injection at metal-organic interfaces often limits the electric current in organic light-emitting diodes without additional injection layers. Integrated nanopatterned electrodes may provide a way to overcome this current injection limit by local field enhancements leading to locally space charge-limited currents. We compare electrical characteristics of planar and nanopatterned hole-only devices based on the charge transport material NPB with different thicknesses in order to investigate the nanopattern's effect on the current limitation mechanism. Integration of a periodic nanograting into the metal electrode yields a current increase of about 1.5–4 times, depending on thickness and operating voltage. To verify the experimental results, we implement a finite element simulation model that solves the coupled Poisson and drift-diffusion equations in a weak form. It includes space charges, drift and diffusion currents, nonlinear mobility, and charge injection at the boundaries. We find in experiment and simulation that the planar devices exhibit injection-limited currents, whereas the currents in the nanopatterned devices are dominated by space charge effects, overcoming the planar injection limit. The simulations show space charge accumulations at the corners of the nanopattern, confirming the idea of locally space charge-limited currents.

Keywords: charge injection, nanostructure, hole-only device, finite element method, injection-limited current, space charge-limited current, organic semiconductor

(Some figures may appear in colour only in the online journal)

1. Introduction

Organic light-emitting diodes (OLEDs) are thin-film surface emission light sources that can be used for a wide range of applications, including displays [1, 2], general lighting [3, 4], and sensing [5–7]. Conventional high-performance OLEDs comprise several layers designed specifically to improve charge carrier injection and transport. These complex multi-layer stacks are commonly fabricated using expensive vacuum processes, which are highly inefficient with regard to material utilization [8]. Towards high-throughput, cost-efficient fabrication methods, such as roll-to-roll printing techniques, a reduction in the number of layers and stack complexity—while maintaining high device performance—is necessary.

Common approaches to enhance the charge injection include blending the organic semiconductor compounds with nanoparticles and inserting interfacial dipole layers at the electrodes [9–12]. While these designs provide effective ways to obtain sufficiently high injection currents, they also increase the

* Author to whom any correspondence should be addressed.

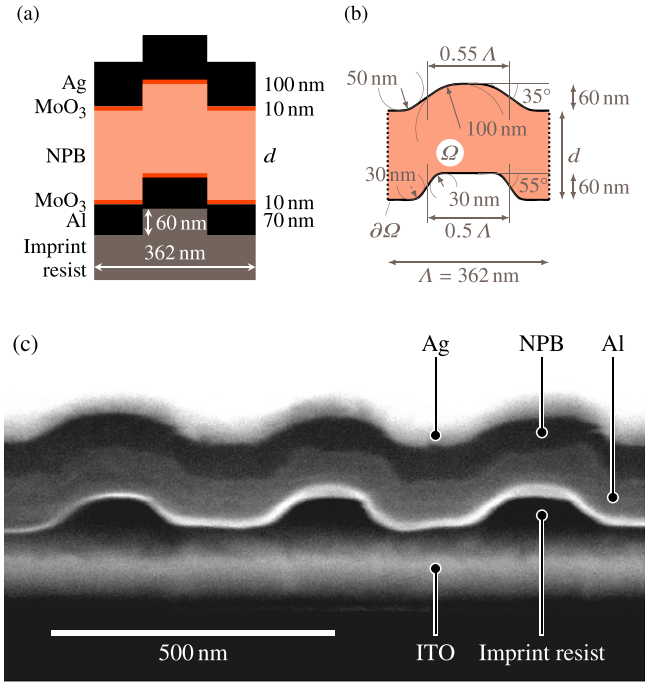

Figure 1. Overview of the investigated nanopatterned hole-only devices' geometry. (a) Schematic of the layer stack. (b) Geometric definition of the simulated domain Ω and its boundary $\partial\Omega$ in the FEM model. We used the cross-section image shown in (c) to determine the geometry for the simulations. Note that the simulated geometry is slightly idealized as it does not include surface irregularities. (c) Scanning electron microscope (SEM) image of the cross-section of a nanopatterned aluminium-NPB-silver hole-only device. The sample for this measurement has been fabricated on ITO-coated glass to achieve better substrate conductivity for imaging. The cross-section was created with a focused ion beam on a Helios Nanolab 600 SEM. It shows that the Al-NPB interface preserves the trapezoidal shape of the original pattern in the imprint resist layer (with rounded edges), whereas the NPB-Ag interface has a smoother sine-like shape.

complexity of the device structure and require additional processing steps. An alternative approach to increase the injected current, overcoming the need of dedicated injection layers, is based on local field enhancement. In order to explore its suitability for current injection at metal-organic interfaces, we investigate the effect of periodically nanopatterned electrodes (see figure 1(c) for an SEM image) on the charge injection and the current limitation mechanism in organic semiconductor devices.

Electrodes with integrated nanostructures have been shown to improve the performance of organic semiconductor devices such as OLEDs [13–15], organic solar cells [16, 17], and organic field-effect transistors [18]. However, performance enhancement is usually not only due to nanostructure-induced charge injection but may include additional electrical, optical, geometrical, and morphological effects. For organic solar cells, several combined electrical and optical studies on the impact of nanopatterned electrodes on light absorption and charge extraction have been reported [19, 20], whereas reports on the electrical properties of nanopatterned OLEDs are scarce and focus mainly on devices limited exclusively by charge injection [21, 22].

In contrast, we investigate devices in which the electrode's nanopattern facilitates the transition from injection-limited to space charge-limited operation. By comparing the current–voltage characteristics of simplified single-carrier devices, we show that the current increase in nanopatterned devices strongly depends on the interplay between charge injection properties of the electrode and the organic semiconductor layer thickness. In order to identify injection-limited and space charge-limited regimes and quantify the contribution of the nanopattern, we employ a simulation model using the finite element method (FEM) including charge injection properties at the metal-organic interface as well as (field-dependent) charge transport properties of the organic semiconductor. The simulation not only allows for accurate modelling of the charge carrier and electric field distributions inside the devices, but also takes into account possible changes in the current limitation mechanism.

2. Charge injection and charge transport

Organic semiconducting materials used in optoelectronic devices usually exhibit high band gap energies between 2 and 4 eV preventing thermal excitation of charge carriers. As these materials possess practically no intrinsic free charge carriers at room temperature, their electrical conductivity instead relies on the injection of excess charges [23]. The current flow in a single-carrier device when exposed to an external bias voltage may therefore be limited by the charge injection from the electrode into the semiconductor or the organic layer's charge transport capability (including potential trap states) [24]. Injection of charge carriers is typically impeded by an energy barrier ΔW between the electrode's Fermi level and the charge transport level in the organic material. In the case of a high external electric field, charge injection is usually assumed to be dominated by quantum tunnelling of charge carriers through the injection barrier [25]. Considering a triangular barrier given by the superposition of the unreduced injection barrier and the applied field E, the Fowler–Nordheim (FN) model predicts the injection current to follow the form [26]

$$J = A_{\mathrm{FN}} \frac{E^2}{\Delta W} \exp\left(-\beta_{\mathrm{FN}} \frac{\sqrt{\Delta W^3}}{E} \right). \tag{1}$$

At lower fields, injection of thermally activated charge carriers across the barrier, as described by Richardson [27] and Dushman [28], plays an important role. The injected charges' image potentials, superimposed with the externally applied electric potential, causes a field-dependent reduction of the injection barrier, which is known as the Schottky effect [29]. This injection mechanism is referred to as Richardson–Schottky (RS) thermionic emission. The corresponding injection current is given by [30]

$$J = A_{\mathrm{RS}} T^2 \exp\left(-\frac{\Delta W}{k_{\mathrm{B}} T} \right) \exp(\beta_{\mathrm{RS}} \sqrt{E}). \tag{2}$$

The effective barrier height depends on the electric field at the electrode surface. At higher electric fields, the maximum of the potential energy curve is located closer to the electrode

surface, resulting in a stronger reduction of the initial injection barrier ΔW by the image potential.

If the injected current is higher than the maximum current supported by the semiconductor's transport properties, charge carriers accumulate at the electrode-semiconductor interface and form a space charge counteracting the external electric field. The resulting space charge-limited current (SCLC) mainly depends on the charge carrier mobility μ as well as the spatial and energetic distribution of trap states. In many organic semiconductors, μ is found to show a strong field dependence, often following the Poole–Frenkel form

$$\mu(E) = \mu_0 \exp(\beta\sqrt{E}), \tag{3}$$

where μ_0 is the zero-field mobility [31]. Consequently, a general analytic expression for the SCLC is not readily available. For the simplified case of a trap-free single-carrier current, the current can be approximated as a function of the applied voltage V and the organic layer thickness d according to the Mott–Gurney equation modified by the field-dependent mobility [32, 33]:

$$J = \frac{9}{8}\varepsilon\mu_0\frac{V^2}{d^3}\exp\left(0.891\beta\sqrt{\frac{V}{d}}\right). \tag{4}$$

If an exponential trap distribution is considered, the current follows a power law

$$J \propto \frac{V^{\ell+1}}{d^{2\ell+1}}, \tag{5}$$

where the parameter ℓ is given by the trap distribution [34].

Space charge-limited currents are typically observed in organic semiconducting layers with high thickness (up to several hundreds of nanometres) and low mobility. In high-performance device stacks, however, thin layers of highly optimized charge transport materials are used, suggesting that currents may be predominantly injection limited if no dedicated charge injection layers are employed. For spatially homogeneous devices, different techniques for identifying the dominant current limitation mechanism have been reported [30, 35–38]. A simple method to distinguish between injection-limited current (ILC) and space charge-limited current utilizes the dependence of the current on the organic layer thickness at constant average electric field (V/d = const.). As can be seen from (1) and (2), purely injection-limited current does not show any thickness dependence:

$$J(V/d = \text{const.}) \neq f(d). \tag{6}$$

Trap-free SCLC, on the other hand, scales with the inverse of the layer thickness:

$$J(V/d = \text{const.}) \propto d^{-1}. \tag{7}$$

This criterion is valid if the carrier mobility does not depend on the electric field and also for a Poole–Frenkel field-dependent mobility, as can be seen from equation (4). For trap-limited SCLC with a statistical trap state distribution, the current density follows the form

$$J(V/d = \text{const.}) \propto d^{-\ell} \quad \text{with } \ell > 1. \tag{8}$$

This approach, however, is no longer valid in nanopatterned layer stacks where local field enhancements may affect the current limitation mechanism. In order to identify SCLC regimes in otherwise injection-limited devices, spatially resolved modelling of the device structure including the electric field distribution and charge carrier density is necessary.

3. Experimental

We fabricated hole-only devices (HODs) with different electrode configurations and organic layer thicknesses using the well-known organic semiconductor NPB (N,N′-Di(1-naphthyl)-N,N′-diphenyl-(1,1′-biphenyl)-4,4′-diamine) as the hole transport material. Nanopatterning of the samples was performed by UV nanoimprint lithography (UV NIL), as described by Jahns *et al* [39]. A one-dimensional nanograting with grating period $\Lambda = 370$ nm and grating depth $d = 60$ nm fabricated by laser interference lithography was employed as the master template for the nanopatterning process. This primary nanograting was replicated into a secondary imprint stamp consisting of the flexible silicone PDMS (polydimethylsiloxane) which was used in the actual imprint step. For this purpose, a mixture of Sylgard 184 (Dow Corning) and the corresponding curing agent (mixing ration 8:1) was poured onto the glass master template and cured at 130 °C for 20 min. Due to thermal shrinkage of the silicone, the period length of the secondary stamp was reduced to 362 nm. For the NIL process, a 200 nm thick layer of the UV-curable imprint resist Amonil MMS4 (Amo GmbH) was spin-coated onto a 25×25 mm^2 glass substrate. The PDMS stamp was subsequently pressed onto the sample surface in order to transfer the nanograting into the imprint resist. After curing the resist by UV illumination for 80 s, the imprint stamp was removed, revealing a replica of the master nanograting on the surface of the glass substrate.

The Al bottom electrode as well as the following semiconducting layers and the Ag top electrode were thermally evaporated onto the nanopatterned imprint resist, resulting in 1D grating-patterned electrode-semiconductor interfaces for charge injection into the devices, as shown schematically in figure 1(a). A 10 nm thin layer of the hole injection/electron blocking material MoO_3 was deposited between the hole transport layer and both electrodes to prevent electron injection which would lead to charge recombination inside the device [40]. Planar HODs holding no grating pattern were fabricated as reference devices by evaporating the device layers directly onto the surface of polished glass substrates. Each sample substrate held 16 identical HODs, half of which had an active device area of 1×1 mm^2 while the other half had an active device area of 2×2 mm^2. J–V curves were recorded using a source measurement unit (Keithley SourceMeter 2450) at sufficiently slow measurement intervals to avoid transient effects [41].

4. Modelling

The model includes Gauß' law, the continuity equation, and nonlinear equations for the charge carrier mobility and the charge injection. The first two equations read

$$\operatorname{div} \varepsilon \vec{E} = q n_{\mathrm{h}} \tag{9}$$

and

$$\operatorname{div} \vec{J} = 0, \tag{10}$$

where $\vec{E}$ can be expressed via the electric potential ϕ and the current density $\vec{J}$ is composed of drift and diffusion currents:

$$\vec{E} = -\operatorname{grad} \phi, \tag{11}$$

$$\vec{J} = q n_{\mathrm{h}} \mu \vec{E} - qD \operatorname{grad} n_{\mathrm{h}}. \tag{12}$$

Here, q is the elementary charge, n_{h} denotes the hole density, $\varepsilon = \varepsilon_0 \varepsilon_{\mathrm{r}}$ the dielectric constant, μ the (nonlinear) hole mobility, and D the hole diffusion constant. We use the Einstein relation $qD/\mu = k_{\mathrm{B}}T$, although its validity for organic semiconductors can be questioned [42–44].

In order to solve these coupled nonlinear equations for the 2D nanopatterned geometry shown in figure 1(b), we implemented them using the weak form PDE solver in COMSOL Multiphysics. Multiplying equations (9) and (10) with the test functions $\tilde{\phi}$ and $\tilde{n}_{\mathrm{h}}$, respectively, integrating over the simulation domain Ω and performing the integration by parts results in

$$\oint_{\partial\Omega} (\varepsilon \vec{E}\, \tilde{\phi}) \cdot \vec{n}\, \mathrm{d}s - \iint_{\Omega} (\varepsilon \vec{E}\, \tilde{\phi}) \cdot \operatorname{grad} \tilde{\phi}\, \mathrm{d}\Omega = \iint_{\Omega} q n_{\mathrm{h}} \tilde{\phi}\, \mathrm{d}\Omega, \tag{13}$$

$$\oint_{\partial\Omega} (\vec{J}\, \tilde{n}_{\mathrm{h}}) \cdot \vec{n}\, \mathrm{d}s - \iint_{\Omega} \vec{J} \cdot \operatorname{grad} \tilde{n}_{\mathrm{h}}\, \mathrm{d}\Omega = 0, \tag{14}$$

where $\vec{E}$ and $\vec{J}$ are inserted from equations (11) and (12). $\vec{n}$ is the outward unit normal vector. The 2D simulation domain Ω and its boundary $\partial\Omega$ are shown in detail in figure 1(b).

The boundary integrals are used to define the boundary conditions: On the left and right boundary (dotted in figure 1(b)), we use zero-flux Neumann conditions ($\vec{E} \cdot \vec{n} = 0$ and $\vec{J} \cdot \vec{n} = 0$). The anode (bottom) boundary is described by the Dirichlet condition $\phi|_{\mathrm{anode}} = \phi_0$ for the potential and the Neumann condition $\vec{J} \cdot \vec{n} = J_{\mathrm{inj}}(E)$ with an electric field-depended injected current density (discussed below). The cathode (top) boundary is set to the Dirichlet conditions $\phi|_{\mathrm{cathode}} = 0$ and $n_{\mathrm{h}}|_{\mathrm{cathode}} = 0$.

Our charge carrier injection model is based on the thermionic Richardson–Dushmann–Schottky-like injection $J_{\mathrm{inj}}(E) = A_{\mathrm{RS}} T^2 \exp(-\Delta W/k_{\mathrm{B}}T) \exp(\beta_{\mathrm{RS}} \sqrt{E})$, but refined using the asymptotic results from Emtage and O'Dwyer [45]:

$$J_{\mathrm{inj}}(E) = \begin{cases} (1 - \operatorname{sig}(E/E_0)) \cdot \alpha_{\mathrm{EO}} E + \\ \operatorname{sig}(E/E_0) \cdot \alpha_{\mathrm{EO}} \sqrt{\dfrac{2}{\pi \beta_{\mathrm{EO}}}}\, E^{3/4} \exp(\beta_{\mathrm{EO}} \sqrt{E}) \end{cases}, \tag{15}$$

where $\operatorname{sig}(x) = x^2/(1 + x^2)$ is a sigmoid function that provides a smooth transition around $E = E_0$ between the two asymptotic solutions. The parameter α_{EO} depends on the injection barrier ΔW as follows: $\alpha_{\mathrm{EO}} \propto \exp(-\Delta W/k_{\mathrm{B}}T)$. However, although an analytic expression for the proportionality factor is given by Emtage and O'Dwyer, it is known that these classical results give quantitatively incorrect results for organic semiconductors [46]. Furthermore, the actual energy barrier at the interface can significantly differ from that calculated from literature values for the energy levels of the individual materials in vacuum [11]. The second parameter in the injection model, β_{EO}, can in theory be calculated from $\beta_{\mathrm{EO}}^2 = q^3/(4\pi\varepsilon k_{\mathrm{B}}^2 T^2)$. We found that the simple closed form expression in equation (15) is a good approximation for the Arkhipov model of charge injection from a metallic electrode into a disordered hopping system [47, 48]. Interfacial trap states can also influence the charge injection [49–51]. In our model it is assumed that such influences are included in the chosen values for α_{EO} and β_{EO}. The feature sizes of the investigated nanostructures ($\gg 10$ nm) are much larger than all relevant molecular distances. Therefore, we assume that a possible distribution of trap states is identical for planar and nanopatterned interfaces. Hence, the same model is used for simulating both device types.

We assume trap-free charge transport in the NPB layer [30, 52], following the Poole–Frenkel field dependence:

$$\mu = \mu(E) = \mu_0 \exp(\beta \sqrt{E}). \tag{16}$$

It has been previously observed that the zero-field mobility of NPB depends on its layer thickness [53, 54]. It is unclear how this effect would influence the nanopatterned NPB. Therefore, we did not include such details into the model.

We used the following parameters for the simulation:

$$\begin{aligned} \alpha_{\mathrm{EO}} &= 20.4 \times 10^{-9}\ \mathrm{S\ m^{-1}}, \\ \mu_0 &= 3.00 \times 10^{-9}\ \mathrm{m^2\ (V\ s)^{-1}}, \\ \beta_{\mathrm{EO}} &= 1.65 \times 10^{-3}\ \sqrt{\mathrm{m/V}}, \\ \beta &= 400 \times 10^{-6}\ \sqrt{\mathrm{m/V}}, \\ E_0 &= 1 \times 10^{7}\ \mathrm{V\ m^{-1}}, \\ \varepsilon_{\mathrm{r}} &= 2.45. \end{aligned} \tag{17}$$

Considering the applied assumptions and simplifications, we did not attempt to obtain these parameters by a precise fitting; they were merely chosen such that model and experiment agree in their general behaviour and to be similar to analytic expressions and values reported in the literature. In addition to the here employed NPB thickness variation, temperature-dependent measurements would offer a way to further optimize the fitting parameters based on their different temperature characteristics [55–58]. This would also allow investigating potential differences in the temperature dependence of nanopatterned and planar devices.

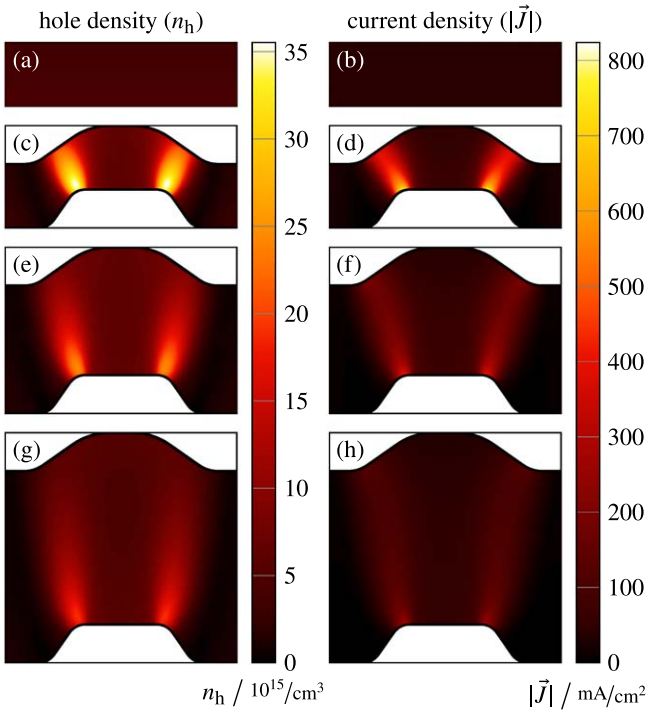

Figure 2. Simulated hole and current densities for different HOD geometries. First row: planar 100 nm thin HODs. Second to fourth row: nanopatterned HODs with 60 nm grating height and 100 nm, 200 nm, and 300 nm organic layer thickness. The fields are calculated for an applied voltage of 2.5 V, 2.5 V, 5.0 V, and 7.5 V, respectively, such that V/d is the same for all four devices. The hole densities are locally strongly increased at the grating's corners.

5. Results and discussion

Simulated hole and current density distributions for different HOD geometries are presented in figure 2. In the planar device, the current density is uniform across the entire organic layer cross-section irrespective of charge injection and charge transport properties. The hole density, on the other hand, may exhibit a gradient from anode (bottom electrode) to cathode depending on whether the current is injection limited or space charge limited. In the 100 nm thin planar HOD, the hole density is nearly constant with $n_h \approx 4 \times 10^{15}$ cm^{-3}, indicating almost exclusively ILC. The current density is $J = 34.7$ mA cm^{-2}. In the nanopatterned devices, electric field intensity is enhanced at the corners of the nanograting due to the sharp features and the reduced inter-electrode distance. The precise field dependence of the current differs at very low and very high fields and can be extracted from equation (15). In the relevant field range, the injected current rises with increasing electric field strength at the metal-semiconductor interface approximately following $J_{inj}(E) \propto \exp(\beta_{EO}\sqrt{E})$. The local increase in charge injection leads to the formation of preferential current paths between the electrodes where the current density is significantly higher than in the surrounding material. The corresponding hole density enhancement along these paths and especially close to the anode indicates a local transition from ILC to SCLC conditions.

Isolated experimental observation of local electric effects is difficult because only current–voltage characteristics of entire devices (corresponding to the integrated current density across the device area), as shown in figure 3, are directly accessible. Still, comparison of different layer thicknesses allows for identification of fully injection-limited current flow as opposed to (locally or globally) bulk-limited currents.

Small instabilities of the J–V characteristics (in the form of irreproducible current spikes) are recognizable for some of the experimental data. These deviations from the ideal smooth curve shape occurred irregularly at low voltages in all experimental samples and were not limited to nanopatterned HODs. We assume the instabilities to be associated with the Al anode as no current spikes were observed for comparable devices comprising a metal oxide electrode. For all thicknesses, the nanopatterned HODs (red curves) exhibit significantly higher current densities than the planar samples. As the impact of nanopattern-induced injection improvement increases with decreasing organic layer thickness, the measured current enhancement ranges from about 4 times for the 100 nm devices to 1.5 times for the 300 nm devices. Although this current enhancement is in agreement with the increase in charge injection visible in the simulation data, the J–V curves alone do not suffice to conclude on the current limitation mechanism.

Instead, the transition from injection-limited to space charge-limited currents can be deduced from the current's thickness dependence. As discussed above, $J(d) = \text{const.}$ for ILC and $J(d) \propto 1/d$ for SCLC when keeping V/d constant. Comparison of the J–V/d curves depicted in figure 4(a) shows that the current density at constant average electric field is effectively independent of the organic layer thickness for the investigated planar HODs (grey lines), confirming that the current is mainly limited by charge injection.

Injection-limited current would be expected for the pristine metal-organic interface, given the high nominal injection barrier of >1 eV between the work function of the Al electrode (3.6–4.3 eV) and the HOMO level of NPB ($\approx$ 5.4 eV) [11, 59–62]. The additional interfacial MoO_3 layer, however, not only serves as an electron blocking layer but also improves hole injection into the organic semiconductor. The underlying physical mechanisms have been under debate for some time and appear to differ depending on the device structure [63, 64]. This is in no small part because the preparation process of the MoO_3 thin film strongly influences its electronic properties [65–67]. Space charge-limited current in organic semiconductor devices featuring comparatively high work function electrodes, such as ITO and Au, with interfacial MoO_3 layers has been attributed to a reduced injection barrier due to favourable energy level alignment, p-type doping of the organic semiconductor and charge generation by electron transfer to the metal oxide [68–70]. Furthermore, the optimal film thickness for charge injection has been shown to be in the range of 1 nm, whereas a higher thickness of up to 20 nm results in significantly lower charge injection enhancement [64, 71]. In the investigated samples, the increased hole injection induced by the 10 nm thick MoO_3 layer is not sufficient to overcome the injection limitation at the Al electrode. Consequently, the planar

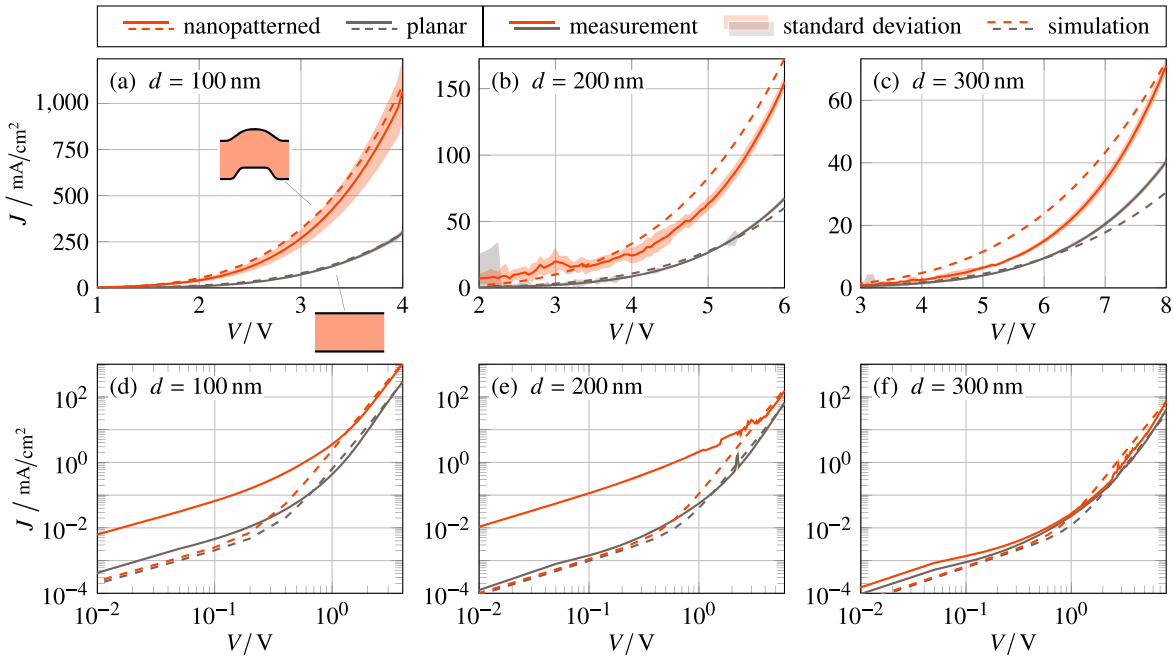

Figure 3. Comparison of measured and simulated J–V curves for unpatterned (grey) and nanopatterned (red) HODs with linear and logarithmic axes. All simulations used the same material parameters. The measurements and simulations agree in the general behaviour for the planar and nanopatterned HODs, showing that the model includes the main physical processes. The differences imply that the model does not cover all contributing physical phenomena. We attribute the large deviations in the very low voltage regime, which can be only seen in the logarithmic plots, to defects in the nanopatterned devices leading to small leakage currents.

devices exhibit ILC for all organic layer thicknesses under investigation.

In contrast, a clear thickness dependence is observable for the J–V/d curves of the nanopatterned HODs (red lines), suggesting that the current is not exclusively injection limited in these devices. However, it must be considered that varying the layer thickness of the nanopatterned devices also changes the relative positions and distances of the adjacent bottom and top grating corners. Due to this geometric effect, even purely injection-limited nanopatterned devices would show a monotonically increasing current dependence on $1/d$ (in contrast to the planar devices' constant ILC). In order to eliminate this effect, we adjusted the operating voltage to compensate geometry-dependent differences in field enhancement: We took the $d = 200$ nm device as a reference point and calculated its injection-limited current (assuming $\mu \to \infty$) as $J = 306\ \mathrm{mA\ cm^{-2}}$ for $V/d = 0.25\ \mathrm{MV\ cm^{-1}}$. Subsequently, we determined the necessary (reduced or increased) voltage to obtain this injection-limited current for all other thicknesses. The resulting operating voltages were then used to simulate the J versus $1/d$ dependence including injection properties and space charge formations, as shown in figure 4(b).

Since the planar devices are not affected by geometric effects, no voltage compensation is required and the corresponding curves are shown for $V/d = 0.25\ \mathrm{MV\ cm^{-1}} = \mathrm{const}$. As discussed above, the fabricated planar devices show a pure ILC behaviour close to the injection limit. Although a slight roll-off towards larger thicknesses is observable in the simulation results, the currents are still predominantly injection limited. This slight discrepancy between measurement and simulation may be attributed to thickness-dependent morphological effects in the NPB or deviations in the fabrication process that are not reproduced in the model.

The nanopatterned devices, on the other hand, exhibit a clear and approximately linear current increase with $1/d$, overcoming the planar injection limit—even under decreasing V/d to compensate the geometric effects. This proves that the limiting factor on the current is indeed not the injection, because the red curve in figure 4(b) would be nearly constant if charge injection was the main current limitation mechanism. Instead, the almost linear current increase indicates that space charge accumulation is the dominant effect.

The J–V and J–$1/d$ characteristics shown in figures 3 and 4 only allow for identification of the current-limiting mechanisms on the device level. In order to illustrate the local transition from injection-limited to space charge-limited currents at the nanopattern, we simulated the 200 nm nanopatterned HOD assuming significantly higher and lower hole mobilities than those of NPB, as shown in figure 5. In the case of very large mobility, the current is injection limited over the whole device: The charge density—although enhanced at the corners—shows no accumulation towards the anode and, consequently, the current enhancement through the nanopattern is high. On the other hand, in the case of very low mobility, the current is space charge limited over the whole device: The space charges accumulate towards the anode both at the corner and at the centre. Therefore, the current enhancement through the nanopattern is low due to limited mobility and strong field reduction.

For medium mobility, however, space charges accumulate only at the corners, leading to a locally space charge-

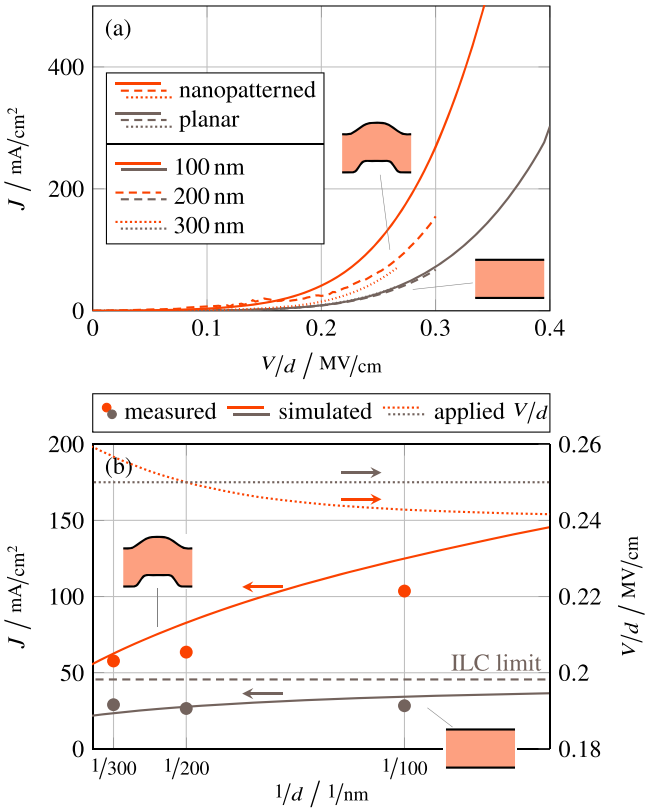

Figure 4. ILC versus SCLC analysis. (a) Measured J–V/d curves for all three thicknesses. The curves for the unpatterned devices are nearly identical, clearly indicating ILC behaviour. For the nanopatterned devices, a distinct separation between the curves is visible, indicating a more space charge-limited behaviour. (b) Measured (circles) and simulated (solid lines) thickness-dependent current densities at the specified applied voltages (dotted curves). For the nanopatterned devices, V/d is chosen such that geometrical effects of the thickness variation are compensated. The planar devices (grey circles, grey line) show barely any thickness dependence at constant V/d, indicating a predominantly injection-limited current. In contrast, the nanopatterned devices (red circles, red line) show an approximately linear current dependence on $1/d$, indicating that the current is mainly space charge-limited.

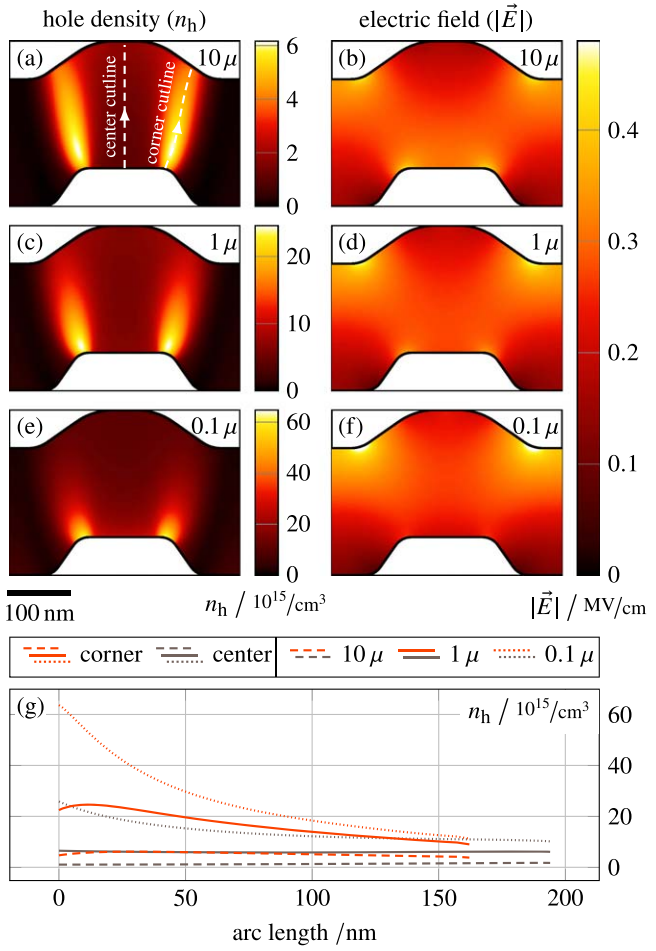

Figure 5. Local current-limiting mechanisms. (a)–(f) Simulated hole densities (left column) and electric fields (right column) in the 200 nm nanopatterned HOD for different mobilities (0.1×, 1×, and 10× the mobility given in equation (17)). Note the different colour scales in the hole density plots. The electric field plots show increasing field reduction at the corners from (b) over (d) to (f) in accordance with the increased local charge accumulation in (c) and (e). The charge density in (a) is low in general and shows barely any gradient towards the anode. (g) Line plots of the hole density along the two cutlines shown in (a), emanating from the grating's centre and corner, respectively.

limited current. This corresponds to the incipient field reduction at the corners in figure 5(d) compared to (b). In contrast, there is no space charge gradient towards the anode at the centre, which means that the current is still injection limited in areas without field enhancement.

As a result, the largest increase in current injection through a nanopattern can be expected when the mobility is high. If the current starts to be locally space charge limited, the device performance will benefit more from improving the mobility than from further injection enhancement.

6. Conclusion

In conclusion, we have investigated the impact of integrated nanopatterns on charge injection and current limitation mechanisms at a metal electrode in organic semiconductor devices. In unpatterned HODs employing NPB as the hole-transport layer and Al as the anode, the current is nearly exclusively injection limited for the investigated organic layer thicknesses (100 nm, 200 nm, and 300 nm). The integration of a nanopattern at the electrode interface leads to field enhancement at the grating corners, locally increasing the current density. As a result, current throughout the device is no longer purely injection limited, but shows predominantly space charge-limited behaviour. The transition from the ILC regime to the SCLC regime can be explained by local charge injection enhancement due to the nanopattern. We believe these findings to be a promising approach towards high performance OLED device stacks omitting dedicated charge injection layers.

Acknowledgments

The authors acknowledge support by Interreg (Project Rollflex, 1_11.12.2014).

Data availability statement

The data that support the findings of this study are available upon reasonable request from the authors.

Author contributions

J Buhl and H Lüder contributed equally to this work. J Buhl developed the manufacturing process, fabricated and characterized the samples. H Lüder developed, implemented and ran the FEM simulations. Both authors wrote the manuscript. M Gerken developed the concept, acquired funding, supervised the research, reviewed and edited the manuscript. All authors discussed and interpreted the results.

ORCID iDs

Janek Buhl https://orcid.org/0000-0001-6633-5741
Hannes Lüder https://orcid.org/0000-0002-3289-5086
Martina Gerken https://orcid.org/0000-0002-4234-7833

References

[1] Huang Y, Hsiang E L, Deng M Y and Wu S T 2020 *Light Sci. Appl.* **9** 1–16
[2] Joo W J *et al* 2020 *Science* **370** 459–63
[3] Park J W, Shin D C and Park S H 2011 *Semicond. Sci. Technol.* **26** 034002
[4] Pode R 2020 *Renew. Sustain. Energy Rev.* **133** 110043
[5] Choudhury B, Shinar R and Shinar J 2004 *J. Appl. Phys.* **96** 2949
[6] Liu R, Cai Y, Park J M, Ho K M, Shinar J and Shinar R 2011 *Adv. Funct. Mater.* **21** 4744–53
[7] Titov I, Köpke M, Schneidewind N C, Buhl J, Murat Y and Gerken M 2020 *IEEE Sens. J.* **20** 7540–7
[8] Ho S, Liu S, Chen Y and So F 2015 *J. Photon. Energy* **5** 057611
[9] Khan M R, Jagtap A M, Koteswara Rao K S R and Menon R 2019 *Org. Electron.* **69** 361–6
[10] Park J W, Ullah M H, Park S S and Ha C S 2007 *Mater. Sci. Mater.* **18** 393–7
[11] Ishii H, Sugiyama K, Ito E and Seki K 1999 *Adv. Mater.* **11** 605–25
[12] Ding X M, Hung L M, Cheng L F, Deng Z B, Hou X Y, Lee C S and Lee S T 2000 *Appl. Phys. Lett.* **76** 2704–6
[13] Lupton J M, Matterson B J, Samuel I D, Jory M J and Barnes W L 2000 *Appl. Phys. Lett.* **77** 3340
[14] Geyer U, Hauss J, Riedel B, Gleiss S, Lemmer U and Gerken M 2008 *J. Appl. Phys.* **104** 93111
[15] Li Y *et al* 2019 *Nat. Commun.* **10** 2972
[16] Min C, Li J, Veronis G, Lee J Y, Fan S and Peumans P 2010 *Appl. Phys. Lett.* **96** 133302
[17] Beck J H, Ray B, Grote R R, Osgood R M, Black C T, Alam M A and Kymissis I 2014 *IEEE J. Photovolt.* **4** 1100–6
[18] Ji D, Wang Y, Chi L and Fuchs H 2015 *Adv. Funct. Mater.* **25** 3855–9
[19] Ray B, Khan M R, Black C and Alam M A 2013 *IEEE J. Photovolt.* **3** 318–29
[20] Mirsafaei M, Fallahpour A H, Lugli P, Rubahn H G, Adam J and Madsen M 2017 *Sci. Rep.* **7** 5300
[21] Fujita M, Ueno T, Ishihara K, Asano T, Noda S, Ohata H, Tsuji T, Nakada H and Shimoji N 2004 *Appl. Phys. Lett.* **85** 5769–71
[22] Fujita M, Ishihara K, Ueno T, Asano T, Noda S, Ohata H, Tsuji T, Nakada H and Shimoji N 2005 *Jpn. J. Appl. Phys.* **44** 3669
[23] Müllen K and Scherf U 2006 *Organic Light Emitting Devices: Synthesis, Properties and Applications* (Weinheim: Wiley-VCH)
[24] Köhler A and Bässler H 2015 *Electronic Processes in Organic Semiconductors* (Weinheim: Wiley-VCH)
[25] Wang Z B, Helander M G, Greiner M T, Qiu J and Lu Z H 2010 *J. Appl. Phys.* **107** 034506
[26] Fowler R H and Nordheim L 1928 *Proc. R. Soc. Lond.* **119** 173–81
[27] Richardson O 1914 *Phil. Mag.* **28** 633–47
[28] Dushman S 1923 *Phys. Rev.* **21** 623–36
[29] Schottky W 1914 *Phys. Z.* **15** 872–8
[30] Brütting W, Berleb S and Mückl A G 2001 *Org. Electron.* **2** 1–36
[31] Blom P M, de Jong M J M and Liedenbaum C T 1998 *Polym. Adv. Technol.* **9** 390–401
[32] Mott N F and Gurney R W 1940 *Electronic Processes in Ionic Crystals* (Oxford: Clarendon)
[33] Murgatroyd P N 1970 *J. Phys. D: Appl. Phys.* **3** 151–6
[34] Bässler H 1998 *Polym. Adv. Technol.* **9** 402–18
[35] Giebeler C, Antoniadis H, Bradley D D and Shirota Y 1998 *Appl. Phys. Lett.* **72** 2448
[36] Torricelli F, Zappa D and Colalongo L 2010 *Appl. Phys. Lett.* **96** 113304
[37] Juška G, Nekrašas N and Genevičius K 2012 *J. Non-Cryst. Solids* **358** 748–50
[38] Züfle S, Altazin S, Hofmann A, Jäger L, Neukom M T, Schmidt T D, Brütting W and Ruhstaller B 2017 *J. Appl. Phys.* **121** 175501
[39] Jahns S, Bräu M, Meyer B O, Karrock T, Gutekunst S B, Blohm L, Selhuber-Unkel C, Buhmann R, Nazirizadeh Y and Gerken M 2015 *Biomed. Opt. Express* **6** 3724–36
[40] Lee H, Cho S W, Han K, Jeon P E, Whang C N, Jeong K, Cho K and Yi Y 2008 *Appl. Phys. Lett.* **93** 043308
[41] Sajedi Alvar M, Blom P W M and Wetzelaer G J A H 2020 *Nat. Commun.* **11** 1–9
[42] Wetzelaer G J A H, Koster L J A and Blom P W M 2011 *Phys. Rev. Lett.* **107** 066605
[43] Li L, Meller G and Kosina H 2009 *J. Appl. Phys.* **106** 013714
[44] Li L, Lu N, Liu M and Bässler H 2014 *Phys. Rev.* B **90** 214107
[45] Emtage P R and O'Dwyer J J 1966 *Phys. Rev. Lett.* **16** 356–8
[46] Wolf U, Arkhipov V I and Bässler H 1999 *Phys. Rev.* B **59** 7507–13
[47] Arkhipov V I, Emelianova E V, Tak Y H and Bässler H 1998 *J. Appl. Phys.* **84** 848–56
[48] Arkhipov V I, Wolf U and Bässler H 1999 *Phys. Rev.* B **59** 7514–20
[49] Haneef H F, Zeidell A M and Jurchescu O D 2020 *J. Mater. Chem.* C **8** 759–87
[50] Govor L V, Reiter G and Parisi J 2016 *J. Phys. D: Appl. Phys.* **49** 135306
[51] Sen S and Manik N B 2021 *J. Phys. Commun.* **5** 095010
[52] Tsung K K and So S K 2008 *Appl. Phys. Lett.* **92** 103315
[53] Chu T Y and Song O K 2007 *Appl. Phys. Lett.* **91** 073508
[54] Chu T Y and Song O K 2008 *J. Appl. Phys.* **104** 023711
[55] Dacuña J and Salleo A 2011 *Phys. Rev.* B **84** 195209
[56] Fishchuk I I, Kadashchuk A K, Genoe J, Ullah M, Sitter H, Singh T B, Sariciftci N S and Bässler H 2010 *Phys. Rev.* B **81** 045202

[57] Moiz S A, Ahmed M M, Karimov K h S and Mehmood M 2007 *Thin Solid Films* **516** 72–7
[58] Ng T N, Silveira W R and Marohn J A 2007 *Phys. Rev. Lett.* **98** 066101
[59] Matsushima T, Jin G H and Murata H 2008 *J. Appl. Phys.* **104** 054501
[60] Uda M, Nakamura A, Yamamoto T and Fujimoto Y 1998 *J. Electron Spectrosc. Relat. Phenom.* **88-91** 643–8
[61] Park S M, Kim Y H, Yi Y, Oh H Y and Won Kim J 2010 *Appl. Phys. Lett.* **97** 063308
[62] Xie Z T, Ding B F, Gao X D, You Y T, Sun Z Y, Zhang W H, Ding X M and Hou X Y 2009 *J. Appl. Phys.* **105** 106105
[63] Gwinner M C, Pietro R D, Vaynzof Y, Greenberg K J, Ho P K H, Friend R H and Sirringhaus H 2011 *Adv. Funct. Mater.* **21** 1432–41
[64] Haitao X and Xiang Z 2013 *J. Appl. Phys.* **114** 244505
[65] Kanai K, Koizumi K, Ouchi S, Tsukamoto Y, Sakanoue K, Ouchi Y and Seki K 2010 *Org. Electron.* **11** 188–94
[66] Meyer J, Shu A, Kröger M and Kahn A 2010 *Appl. Phys. Lett.* **96** 133308
[67] White R T *et al* 2016 *Sci. Rep.* **6** 21109
[68] Waldrip M, Jurchescu O D, Gundlach D J and Bittle E G 2020 *Adv. Funct. Mater.* **30** 1904576
[69] Choi S, Fuentes-Hernandez C, Wang C Y, Khan T M, Larrain F A, Zhang Y, Barlow S, Marder S R and Kippelen B 2016 *ACS Appl. Mater. Interfaces* **8** 24744–52
[70] Kröger M, Hamwi S, Meyer J, Riedl T, Kowalsky W and Kahn A 2009 *Appl. Phys. Lett.* **95** 123301
[71] Matsushima T, Jin G H, Kanai Y, Yokota T, Kitada S, Kishi T and Murata H 2011 *Org. Electron.* **12** 520–8